

The Rest-Frame Golenetskii Correlation via a Hierarchical Bayesian Analysis

J. Michael Burgess^{1,2*}

¹*The Oskar Klein Centre for Cosmoparticle Physics, SE-106 91 Stockholm, Sweden*

²*Department of Physics, KTH Royal Institute of Technology, AlbaNova, SE-106 91 Stockholm, Sweden*

Accepted XXXX December XX. Received XXXX December XX; in original form XXXX October XX

ABSTRACT

Gamma-ray bursts (GRBs) are characterised by a strong correlation between the instantaneous luminosity and the spectral peak energy within a burst. This correlation, which is known as the hardness-intensity correlation or the Golenetskii correlation, not only holds important clues to the physics of GRBs but is thought to have the potential to determine redshifts of bursts. In this paper, I use a hierarchical Bayesian model to study the universality of the rest-frame Golenetskii correlation and in particular I assess its use as a redshift estimator for GRBs. I find that, using a power-law prescription of the correlation, the power-law indices cluster near a common value, but have a broader variance than previously reported ($\sim 1 - 2$). Furthermore, I find evidence that there is spread in intrinsic rest-frame correlation normalizations for the GRBs in our sample ($\sim 10^{51} - 10^{53}$ erg s⁻¹). This points towards variable physical settings of the emission (magnetic field strength, number of emitting electrons, photospheric radius, viewing angle, etc.). Subsequently, these results eliminate the Golenetskii correlation as a useful tool for redshift determination and hence a cosmological probe. Nevertheless, the Bayesian method introduced in this paper allows for a better determination of the rest frame properties of the correlation, which in turn allows for more stringent limitations for physical models of the emission to be set.

Key words: (stars:) gamma ray bursts – methods: data analysis – methods: statistical

1 INTRODUCTION

A key feature of gamma-ray bursts (GRBs) is the observed relation within a burst between the luminosity and the νF_ν peak energy ($E_{\text{peak}}^{\text{rest}}$) (Golenetskii et al. 1983; Kargatis 1994; Borgonovo & Ryde 2001; Ryde et al. 2006; Ghirlanda et al. 2010; Lu et al. 2010; Zhang & Chen 2012; Guiriec et al. 2013; Burgess et al. 2014). This luminosity- $E_{\text{peak}}^{\text{rest}}$ relation was first discovered by Golenetskii et al. (1983) and has been found in several GRBs regardless of their lightcurve shape. The relation is sometimes referred to as the hardness-intensity correlation or the Golenetskii correlation (GC). It is typically stronger during the decay phase of a GRB lightcurve. The form of the GC states that the luminosity of the GRB is proportional to its $E_{\text{peak}}^{\text{rest}}$ to some power γ :

$$L \propto (E_{\text{peak}}^{\text{rest}})^\gamma \text{ erg s}^{-1} \quad (1)$$

Historically, the GC has been used in an attempt to understand the physical process generating the observed emis-

sion (e.g. Dermer 2004; Ryde et al. 2006; Bošnjak & Daigne 2014). Ryde et al. (2006) pointed out that the correlation is strongest in GRBs with single non-overlapping pulses.

Such a correlation should be a signature of the evolving radiative process occurring in an outflow. For example, if the emission is purely photospheric then one would expect $L \propto \sigma_B T^4$ where σ_B is the Boltzmann constant and $E_{\text{peak}} \propto 3T$ where T is the temperature of the outflow plasma. This fact motivated the original research into photospheric emission of GRBs. Borgonovo & Ryde (2001); Ryde et al. (2006) used single- and multi-component spectral models composed of thermal and non-thermal components to analyze several GRBs and obtain their GCs. It was found that the GCs of these bursts exhibit a wide range of γ (see also Burgess et al. 2014) and it is difficult to assign a common physical setting to all GRBs: it is known that photospheric emission can take on several forms due to the differences in viewing angle (Lundman et al. 2014) as well as subphotospheric dissipation (e.g. Pe’er et al. 2005; Beloborodov 2010) or jet composition (Giannios 2006; Bégue & Pe’er 2015). These advanced photospheric models have just begun mak-

* E-mail: jamesb@kth.se (JMB)

ing predictions to explain the GC (Fan et al. 2012; López-Cámara et al. 2014).

Other attempts to explain the observed GCs invoked non-thermal synchrotron emission (Zhang & Meszaros 2002; Dermer 2004) in both single (Ghirlanda et al. 2010) and multi-component (Burgess et al. 2014; Preece et al. 2014) time-resolved spectra. For synchrotron emission, one expects $L \propto N_e B^2 \Gamma^2 \gamma_e^2$ and $E_{\text{peak}} \propto B \Gamma \gamma_e^2$ where N_e is the number of emitting electrons, B in the magnetic field, γ_e is the characteristic electron Lorentz factor and Γ is the bulk Lorentz factor. This implies that $L \propto N_e E_{\text{peak}}^2 \gamma_e^{-2}$. Deeper considerations for the evolution of the parameters can lead to different γ 's (see Dermer (2004) for examples.) Yet again, the wide range of observed γ 's make it difficult to explain all GRBs with synchrotron emission.

Another feature of the GC exploits the fact that if the relation is generated by a common process, then GCs can be used to estimate redshift of GRBs (Guiriec et al. 2013, 2015). Several GRBs with known redshift exhibited a common rest-frame proportionality constant ($N \simeq 10^{53} \text{ erg s}^{-1}$) between luminosity and $E_{\text{peak}}^{\text{rest}}$. If this is true for all GRBs, it could be possible to use the observer-frame normalization of the relation to estimate the redshifts of GRBs that do not have one measured by other means. This estimation of redshift differs from that of the so-called Amati and Yonetoku relations (Amati et al. 2002; Yonetoku et al. 2004). These relations rely on the time-integrated properties of GRBs and most likely result from the effects of functional correlation (Massaro et al. 2007) and selection effects (Kocevski 2012). If time-resolved GCs such as those studied herein do allow for the estimation of redshift then this would allow for a very powerful cosmological tool as GRBs can probe the high-redshift universe. However, this possibility heavily relies on the assumption of a common rest-frame normalization, which in both the photospheric and synchrotron models is not predicted.

2 THE RELATION AND THE BAYESIAN MODEL

The GC is given in the rest-frame in Equation 1; however, it is derived from observer-frame time-resolved spectral fits of GRBs. The observed spectra are integrated over energy (10 keV - 40 MeV) to yield the energy flux (F_E) which, assuming isotropic emission, is related to the luminosity via $L = 4\pi d_L^2(z) F_E$. Here, z is the redshift of the GRB and $d_L(z)$ is the luminosity distance. Similarly, $E_{\text{peak}}^{\text{rest}} = E_{\text{peak}}^{\text{obs}}(1+z)$.

Assuming that the time-evolving rest-frame luminosity of GRBs derives from a single inherent relationship given as

$$L = N_{\text{rest}} \left(\frac{E_{\text{peak}}^{\text{rest}}}{100 \text{keV}} \right)^\gamma \text{ erg s}^{-1}, \quad (2)$$

where N_{rest} is a normalization attributed to the intrinsic physics of the emission process, and γ is the GC index again attributed to an intrinsic physical process, we shift into the observer-frame such that

$$F_E = \frac{N_{\text{rest}}}{4\pi d_L^2(z)} \left(\frac{E_{\text{peak}}^{\text{obs}}(1+z)}{100 \text{keV}} \right)^\gamma \text{ erg s}^{-1} \text{ cm}^{-2}. \quad (3)$$

Taking the base-10 logarithm to obtain a linear relationship we have

$$\log(F_E) = \log(N_{\text{rest}}) - \log(4\pi d_L^2(z)) + \gamma \log\left(\frac{E_{\text{peak}}^{\text{rest}}(1+z)}{100 \text{keV}}\right). \quad (4)$$

If one makes the assumption that N_{rest} and γ remain constant or tightly distributed for all GRBs, from this equation one can solve for z . I use this assumption to construct a hierarchical Bayesian model (see for example, Mandel et al. 2011; March et al. 2011; Andreon 2012; Sanders et al. 2015; de Souza et al. 2015, for related uses of hierarchical Bayesian models in astrophysics). For the i^{th} GRB $_i$ we have

$$\log\left(F_E^{i,j}\right) = \log(N_{\text{rest}}) - \log\left(4\pi d_L^2(z^i)\right) + \gamma^i \log\left(\frac{E_{\text{peak}}^{\text{obs},j}(1+z^i)}{100 \text{keV}}\right). \quad (5)$$

Here, j indexes time. Figure 1 demonstrates the model. I will call this model *Mod A*. Henceforth, logarithmic quantities ($\log(N_{\text{rest}})$, $\log(F_E)$, etc.) will be represented as $Q = \log(Q)$ for notational simplicity. Since I choose F_E as the dependent quantity and $E_{\text{peak}}^{\text{obs}}$ as the independent quantity, the measurement error in $E_{\text{peak}}^{\text{obs}}$ must be accounted for following the methods of Dellaportas & Stephens (1995); Andreon & Hurn (2013). I also allow for intrinsic scatter in each GC. The following priors are assumed:

$$\mu_\gamma \sim \mathcal{N}(0, \text{std}(F_E)/\text{std}(E_{\text{peak}}^{\text{obs}})) \quad (6)$$

$$\sigma_\gamma \sim \text{Cauchy}_{(0,\infty)}(0, 2.5) \quad (7)$$

$$\gamma^i \sim \mathcal{N}(\mu_\gamma, \sigma_\gamma) \quad (8)$$

$$\mu_{N_{\text{rest}}} \sim \mathcal{N}(52, 5) \quad (9)$$

$$\sigma_{N_{\text{rest}}} \sim \text{Cauchy}_{(0,\infty)}(0, 2.5) \quad (10)$$

$$N_{\text{rest}}^i \sim \mathcal{N}(\mu_{N_{\text{rest}}}, \sigma_{N_{\text{rest}}}) \quad (11)$$

$$z^i \sim \mathcal{U}(0, 15) \quad (12)$$

$$E_{\text{peak}}^{\text{obs},i,j} \sim \mathcal{N}(E_{\text{peak}}^{\text{obs},i,j}, \sigma_{E_{\text{peak}}^{\text{obs},i,j}}) \quad (13)$$

$$\sigma_{\text{scat}}^{2,i} \sim \text{Cauchy}_{(0,\infty)}(0, 2.5) \quad (14)$$

$$F_E^{i,j} \sim \mathcal{N}(\star, \sigma_{\text{scat}}^i) \quad (15)$$

$$F_E^{i,j} \sim \mathcal{N}(F_E^{i,j}, \sigma_{F_E}^{i,j}) \quad (16)$$

$$(17)$$

Here (\star) indicates the right-hand side of Equation 5. Half-Cauchy distributions were chosen as non-informative proper priors for the variances (Gelman 2006). If a GRB has a known redshift, then it can be fixed in the model which will aid in constraining the hyper-parameters for N_{rest} .

I can further generalize the model by relaxing the assumption of a common N_{rest} and γ and allow separate N_{rest} and γ to be fit without their respective hyper-priors. Therefore, I implement two further models, *Mod B* and *Mod C* which relax the assumption of common γ and common N_{rest} respectively. These models are also detailed in Figure 1 when the *red* and then the *blue* hyper-priors are removed.

The models are implemented in *PyStan* (sta 2015) which is a probabilistic modeling language implementing a Hamiltonian Monte Carlo sampler for full Bayesian inference. The posterior marginal distributions of the parameters obtained from *PyStan* can be analyzed to determine γ^i , N_{rest}^i , and z^i .

The simultaneous fitting of all GCs with linked parameters (e.g. γ^i) of the hierarchical model provides shrinkage of the estimates and, if the data support it, will pull together the estimates as well as assist in better fits of GCs where there is less data. For computational speed, I implement the highly accurate, analytic form of $d_L(z)$ from Adachi & Kasai (2012) in my model.

An alternative approach to determining redshifts is to fit all GCs from GRBs with known redshift together as one data set via a standard fitting tool such as FITEXY (Press 2007). A common, calibration rest-frame normalization (N_{cal}) and slope can be determined. Then, GRBs without known redshift can have their observer-frame GCs fitted to determine their observer-frame normalizations (M_z) which can be solved for redshift (see Section 3.1). However, this approach neglects the robustness of the Bayesian model presented here because in the Bayesian model, all parameters are determined from the data simultaneously accounting for all correlations in the parameters and data.

3 SIMULATIONS

To test the feasibility of this approach, I simulate a set of eight GCs to fit with the model. Starting with a universal relation

$$L^{\text{sim}} = N_{\text{rest}}^{\text{sim}} \left(\frac{E_{\text{peak}}^{\text{rest,sim}}}{100\text{keV}} \right)^{\gamma^{\text{sim}}} \text{ erg s}^{-1} \quad (18)$$

a random number of $E_{\text{peak}}^{\text{rest,sim}}$'s are drawn from a log-uniform distribution. For *Mod A*, $N_{\text{rest}}^{\text{sim}} = 52 \text{ erg s}^{-1}$ and $\gamma^{\text{sim}} = 1.5$ for every synthetic GRB (See Figure 2). For *Mod B* and *Mod C*, γ^{sim} is drawn from $\mathcal{U}(1,2)$ and for *Mod C* $N_{\text{rest}}^{\text{sim}}$ is drawn from $\mathcal{U}(51.7, 52.3)$ (see Figures 3 and 4). Then, L^{sim} is computed for each $E_{\text{peak}}^{\text{rest,sim}}$. A random redshift is assigned and the rest-frame quantities are shifted into the observer-frame. Finally, each observer frame quantity has heteroscedastic error added to it assuming that the noise is normally distributed for both $E_{\text{peak}}^{\text{obs,sim}}$ and $F_{\text{E}}^{\text{sim}}$. No intrinsic scatter is added.

3.1 Simulated GCs with Common N_{rest} and γ : *Mod A*

The set of simulated GCs is fit with *Mod A* assuming that $GRB_1 - GRB_4$ have known redshifts and the remaining GRBs do not. Table 1 details the fits and marginal posterior distributions for all parameters are displayed in Appendix A. The observer-frame relations are well recovered by the model and can be seen in Figure 5. The estimated γ^i are well recovered by the model. The N_{rest}^i are also well fitted even for GRBs that do not have a redshift owing to the shrinkage of the posterior by GRBs with known redshift. There is a tight correlation between μ_γ and $\mu_{N_{\text{rest}}}$ (Figure 6) for the hyper parameters. The estimated unknown redshifts have long tails but are generally estimated well as shown in Figure 7. All of the simulated values are within the 95% highest posterior density intervals (HDIs). Still, the spread in estimated values makes them unusable as a cosmological probe.

Now, I compare to the frequentist approach to see the difference in the methods. This approach requires at least one redshift be known to calibrate the N_{rest} . The same four simulated GCs are used as known redshift GRBs as in the previous sections. The method proceeds in the following fashion:

- The four known redshift GRBs have their *rest-frame* GCs fit via the FITEXY method to determine a calibration value for N_{rest} .
- The GRBs without redshift have their *observer-frame* GCs fit to determine their normalization which is $A = M_z/N_{\text{rest}}$ where M_z is the observer-frame normalization.
- Using the calibration N_{rest} , M_z is solved for and subsequently z is obtained.

Table 2 details the results from the procedure. The calibrated rest-frame normalization is $N_{\text{cal}} = 52 \pm 0.01$ with slope $\gamma = 1.49 \pm 0.014$ (compare these to the simulated values of $N_{\text{rest}} = 52$ and $\gamma = 1.5$) It is important to note that FITEXY has a positive bias on the obtained γ 's, an effect that is well known (e.g. Kelly 2007) and the method's statistical properties are poorly understood. This makes the fitting GCs via the method unreliable at determining the inherent physics in the outflow.

The 1σ errors on redshift are determined numerically by fully propagating the errors from the linear fits of both the calibration and observer-frame fits. The results are displayed in Table 2 The hierarchical Bayesian model performs better at obtaining the simulated γ 's (see Table 1). The redshifts are obtained accurately via FITEXY but with very small errors that do not take into account the full variance of the model and data. Therefore, these errors are likely underestimated. We will see how these under-estimated errors lead to inaccurate redshift predictions in the following sections.

3.2 Simulated GCs with Varying γ : *Mod B*

For simulations where γ^i is varied, *Mod B* is used to fit the data. Similar to *Mod A*, *Mod B* is able to estimate the simulated properties of the GRBs. Table 3 details the results. All parameter marginal posterior distributions are shown in Appendix A. Importantly, the varying values of γ^i are well estimated and the redshifts are found but with higher HDIs than those found with *Mod A* (See Figure 7).

I then proceed to fit the simulated data with FITEXY. The results are in Table 4 and show that the redshifts are inaccurately estimated and the errors are underestimated. Therefore, if there is a distribution of γ^i in real data, this method will give incorrect redshifts but the errors may not encompass the true values..

3.3 Simulated GCs with Varying γ and N_{rest} : *Mod C*

Finally, I test *Mod C* which has no linkage between datasets. The fits are detailed in Table 5 and all parameter marginal posterior distributions are displayed in Appendix A. GRBs with known redshift can easily have N_{rest} estimated but the degeneracy between N_{rest} and z for GRBs without known redshift restricts the ability for N_{rest} to have a compact marginal distribution. As a consequence, Figure 8 shows that

redshift cannot be determined in this model. The model is still able to determine γ^i , though, with broader HDIs. The loss of linkage and information sharing between GRBs with known and unknown redshift in this model makes it not useful for cosmology though if it is the model representing the actual physics of GCs, it can be used on GRBs with known redshift to determine rest-frame properties. Once again, FITEXY is tested (Table 6) and it is found that the redshifts are inaccurately estimated with underestimated errors.

3.4 Reconstructing the Simulated Golenetskii Correlation

Another test of the models is how well they reconstruct the simulated relations in the rest-frame. Essentially, the marginalization over redshift removes the cosmological factors in the GCs and allows for the rest-frame quantities to be calculated with the full variance of the model and data. This is more descriptive than simply shifting the observer-frame quantities into the rest-frame using the estimated and known redshifts.

The process of calculating the rest-frame Golenetskii relation depends on whether or not the redshift for a GRB is known. For GRBs with unknown redshift, I first construct the observed rest-frame $E_{\text{peak}}^{\text{rest}}$'s. Since I model the measurement error of the observer-frame $E_{\text{peak}}^{\text{obs}}$ during the fits, I obtain a distribution for each $E_{\text{peak}}^{\text{obs}}$ based off the data and the model. I propagate the distribution of $E_{\text{peak}}^{\text{obs}}$ and the estimated redshift (z_{est}) to reconstruct $E_{\text{peak}}^{\text{rest}} = E_{\text{peak}}^{\text{obs}}(1 + z_{\text{est}})$. Thus a distribution for $E_{\text{peak}}^{\text{rest}}$ is obtained. Similarly, I propagate the obtained distributions of the marginalized parameters to reconstruct $L = N_{\text{rest}} \left(\frac{E_{\text{peak}}^{\text{rest}}}{100\text{keV}} \right)^{\gamma}$.

For GRBs with known redshift, the process is the same except the measured value of z is used rather than the estimated value. At the end of the process, I have distributions of L and $E_{\text{peak}}^{\text{rest}}$ for each data point of each GRB. Figure 9 displays the results of this process for all three models. Compared with the simulated relations (Figures 2 - 4) all models reconstruct the relation well for both GRBs with known and unknown redshift except *Mod C* which cannot estimate unknown redshifts.

4 APPLICATION TO REAL GRBS

The model is now applied to real data from a sample GRBs that have been analyzed with a multi-component spectral model. It has been claimed that the use of multi-component spectra tighten the observed GC in some GRBs (Guiriec et al. 2015). I therefore use the time-resolved luminosity and E_{peak} from Band function (Band et al. 1993) fits of the sample of GRBs analyzed in Burgess et al. (2014). These GRBs are single pulsed in their lightcurves and were analyzed with physical synchrotron models as well as the empirical Band function. Additionally, the models were analyzed under a multi-component model consisting of a non-thermal component modeled as a Band function and a blackbody. I choose from this sample GRBs 081224A, 090719A, 090809A, 110721A, and 110920A. Three tentative redshifts for GRB 110721A appear in the literature ($z = 0.382, 3.2, 3.512$)

(Berger 2011; Greiner 2011), though none are stringent measurements. Nonetheless, I will assume that the actual value is $z = 3.2$ for consistency with Guiriec et al. (2015).

In Guiriec et al. (2015), GRBs were also analyzed with a multi-component model including GRB 080916C which has measured redshift of $z = 4.24$. I reanalyzed this GRB with the model and time-intervals posed in Guiriec et al. (2015) and added this to my sample. The nearby ($z = 0.34$) GRB 130427A is included as well because of its brightness which allows for several time-intervals to be fit with spectral models. Though in Preece et al. (2014) the GRB was fit with both synchrotron and Band models, only the fits with synchrotron statistically required a blackbody. Therefore, fits from the Band function only are used in this work. Finally, I include multi-component analysis of GRB 141028A which has a well measured redshift of $z = 2.332$ Burgess et al. (2015).

All spectral analysis was carried out with RMFIT¹. The F_E was calculated for the Band function for each time-interval using full error propagation of all spectral parameters including those of the other spectral components to obtain the errors on the F_E (See Appendix B for a discussion on error propagation). I use only Band function fits from the multi-component fits because it is claimed that they provide a better redshift estimator. Finally, it is known that GCs are stronger and possess positive slope in the decay phase of GRB lightcurves. They are typically anti-correlated in the rising portion of the lightcurve, therefore, the rise-phase GC is disregarded for this analysis. With this sample (see Figure 10), I proceed with testing the Bayesian models.

4.1 Results

First, I fit the real GCs with *Mod A*. Table 7 and Figure 11 show the results of the fits. Figure 12 shows some variation in γ^i , but the values are clustered due to the pull of the hyper-parameters of the model. Most importantly, GRBs without known redshift have unconstrained N_{rest}^i resulting in unconstrained redshifts (see Figures 13 and 15). The hyper-parameters from the fits are clustered (Figure 14) due mainly to GRBs with known redshift.

Next, *Mod B* is fit to the data. Table 8 and Figure 16 show the results of the fits. The values of γ^i vary due to the loosening of their hyper-parameter constraint (see Figure 17). Additionally, estimates of N_{rest}^i have tighter constraints than with *Mod A*, yet they are still broad (See Figure 18). However, redshift estimation is still unconstrained though the distributions are peaked at lower redshifts with heavy tails (see figure 19).

Finally, *Mod C* is fit to the data. Table 9 and Figure 20 show the results of the fits. Figures 21 and 22 show that both γ^i and N_{rest}^i vary due to the loosening of hyper-prior constraints, but N_{rest} is again loosely constrained. We expect the estimates of redshift to be unconstrained from simulations and find this in the data as well (see Figure 23).

Now, using the FITEXY method, I find that the calibration $N_{\text{cal}} = 51.17 \pm 0.02$ (compared to $\langle \mu_{N_{\text{rest}}} \rangle = 51.74$ with an HDI of 51.33 – 52.21 for *Mod A*) obtained from fitting the four GRBs with known redshift in the rest-frame with

¹ <http://fermi.gsfc.nasa.gov/ssc/data/analysis/rmfit/>

a common $\gamma = 1.72 \pm 0.02$ (compared to $\langle \mu_\gamma \rangle = 1.49$ with an HDI of 1.35 – 1.67 for *Mod A*). Table 10 reveals that while the method can estimate redshifts precisely, known redshifts are reconstructed inaccurately. It was determined that the errors of this method are likely underestimated via simulations in Section 3.1.

Another option would be to use individual GRBs as calibration sources and estimate known redshift. For each GRB with known redshift, I fit its rest-frame GC to obtain N_{cal} and then proceed as before using only one GRB as the calibration to estimate the known redshifts of the other GRBs. Table 11 shows that the estimated redshifts (columns) depend on which calibration GRB (rows) is used. Regardless of which GRB is used as a calibration source, the estimated redshifts are inaccurate. I conclude that the FITEXY method cannot be used to estimate redshifts.

4.2 The Rest-Frame Golenetskii Relation

I calculate the rest-frame Golenetskii relation for each model using GRBs with known redshift following the procedure in Section 3.4. I exclude GRBs without known redshift due to the inability to calculate rest-frame quantities when the redshift is unconstrained as shown in Figure 24. Figure 25 shows the rest-frame correlation for all models. There is little difference between the models' predictions. Even with the hyper-parameter models, a difference in the individual γ^i and N_{rest}^i is allowed. While γ^i do appear tightly distributed, the N_{rest}^i can vary within an order of magnitude.

5 DISCUSSION

I have presented a hierarchical Bayesian model to test the ability of the Golenetskii correlation (Equation 2) to estimate the redshifts of GRBs. The model incorporates all known variance in both the data and assumptions and therefore provides a robust assessment of the claim that accurate redshifts can be obtained. The model performs well with simulated data. The data are generated under the assumptions of the model, so it is expected, but fitting of the simulations allows for determining the accuracy of the model. The model is able to predict simulated redshifts very accurately as long as the rest-frame normalization of the relations are all the same. If this assumption is dropped, the model is unable to predict redshifts though it can still recover rest-frame properties of GRBs with known redshift.

The method of using FITEXY underestimates the errors on predicted redshifts. More importantly, the method predicts inaccurate redshifts if there is not a common N_{rest} and γ in the rest-frame. Moreover, the inaccurate redshifts will have errors that do not encompass the true redshift. Therefore, I find the method unable to predict redshifts.

When I apply the three Bayesian models to the data, I find that the redshift estimates are all unconstrained. Constrained estimates for N_{rest}^i for GRBs with known redshift and γ^i for all GRBs are recovered. Upon examining the inferred rest-frame Golenetskii relations for GRBs with known redshift, I find that N_{rest}^i are tightly distributed but can vary within an order of magnitude. This is most likely the reason that FITEXY under-predicts known redshift. To investigate this, I simulated 1000 GCs from *Mod C* and fit them with

FITEXY as before. Then, the distribution of the difference between estimated redshift and simulated is examined as a function of the difference between N_{cal} and the simulated N_{rest} (see Figure 26). When N_{cal} underestimates the true N_{rest} , then the redshift can be under-predicted. As can be seen in Tables 7-9, N_{cal} always underestimates N_{rest} and therefore the FITEXY method under predicts the known redshifts in our sample.

This leads us to consider what happens when simulations from *Mod C* (possibly resembling the real GRB sample) are fitted but *Mod A*. We know from Section 3.1 that *Mod A* can perfectly estimate redshifts if it represents the true generative model of the data. Therefore, I simulate data from *Mod C* and fit it with *Mod A*. Figures 27 and 28 show that, like the real data in Section 4, *Mod A* cannot constrain N_{rest} and subsequently redshift when there is not a common N_{rest} . Unfortunately, *Mod C* which is applicable to the data, cannot constrain redshifts. This strongly suggests that there is not a universal Golenetskii correlation in the rest-frame.

The fact that all GRBs *do not* share a common N_{rest} is not surprising. It is established that there are at least two observed mechanisms occurring in GRBs: photospheric (Ryde et al. 2010) and non-thermal emission (Zhang et al. 2015; Burgess et al. 2015). In both of these cases, a variance in N_{rest} is expected. I have shown that variance is not negligible. The choice of spectral model also plays an crucial role in determining the slope and normalization of GCs. The results of Burgess et al. (2014); Iyyani et al. (2015) where a physical synchrotron model was used to fit the spectra of the same GRBs used in this study produced GCs with different slopes than what is found here with empirical spectral models. This is due to the different curvature of these models around the νF_ν peak which results in different E_{peak} 's from the spectral fits.

Theoretical predictions for the rest-frame GC are in their infancy. While weak predictions for γ exist (Zhang & Meszaros 2002; Dermer 2004; Fan et al. 2012; Bošnjak & Daigne 2014), exact solutions have only begun to be formulated. This is due in part to the stochastic nature of GRB lightcurves as well as the limited input knowledge available for use in predicting the exact processes that occur in GRB outflows. It is interesting to note that López-Cámara et al. (2014) predict that photospheric models can have different normalizations in the rest-frame depending on viewing angle. If physical spectra can be fit to the data corresponding to such models, then the subsequently derived GCs could be used to predict viewing angles of GRBs which presents an interesting new tool to study GRB prompt emission mechanisms.

6 CONCLUSIONS

I conclude that the Golenetskii correlation does not possess a common N_{rest} which may have interesting implications for the outflow physics of GRBs but precludes them from being used as redshift estimators under the model posed herein. The Golenetskii correlation fails as a standard candle without an additional predictor. This also precludes the use of GCs to estimate cosmological parameters as the broad HDIs found in this study would be folded into the errors on cosmological parameters making their determination weak and

unconstrained. GCs are useful for discerning the physical emission mechanisms occurring in GRBs and warrant dedicated study. A method similar to the one proposed here can be used to study the observer- and/or rest-frame properties of GCs provided the goal is to understand the properties intrinsic to the GRB.

ACKNOWLEDGMENTS

I would like to thank Johannes Buchner, Michael Betancourt, and Bob Carpenter for helpful discussion and direction on the probabilistic model, `Stan`, and font choice. Additionally, I would like to thank Damien Bégué and Felix Ryde for discussions on the physics of GCs.

I additionally thank the Swedish National Infrastructure for Computing (SNIC) and The PDC Center for High Performance Computing at the KTH Royal Institute of Technology for computation time on the Tegnér cluster via grant PDC-2015-27.

This research made use of `Astropy`, a community-developed core Python package for Astronomy (Astropy Collaboration et al. 2013) as well `Matplotlib`, an open source Python graphics environment (Hunter 2007) and `Seaborn` (Waskom et al. 2015) for plotting.

REFERENCES

- 2015, `PyStan`: the Python interface to Stan, Version 2.7.0
 Adachi M., Kasai M., 2012, *Progress of Theoretical Physics*, 127, 145
 Amati L., et al., 2002, 390, 81
 Andreon S., 2012, in , *Astrostatistical Challenges for the New Astronomy*. Springer New York, New York, NY, pp 41–62
 Andreon S., Hurn M., 2013, *Statistical Analysis and Data Mining: The ...*
 Astropy Collaboration et al., 2013, *A&A*, 558, A33
 Band D., Matteson J., Ford L., 1993, *ApJ*, 413, 281
 Bégué D., Pe’er A., 2015, *ApJ*, 802, 134
 Beloborodov A. M., 2010, *MNRAS*, 407, 1033
 Berger E., 2011, *GCN Circular*
 Borgonovo L., Ryde F., 2001, *ApJ*, 548, 770
 Bošnjak Ž., Daigne F., 2014, *A&A*, 568, A45
 Burgess J. M., Bégué D., Ryde F., Omodei N., Pe’er A., Racusin J. L., Cucchiara A., 2015, *arXiv.org*
 Burgess J. M., et al., 2014, *ApJ*, 784, 17
 de Souza R. S., Hilbe J. M., Buelens B., Riggs J. D., Cameron E., Ishida E. E. O., Chies-Santos A. L., Killedar M., 2015, *Monthly Notices of the Royal Astronomical Society*, 453, 1928
 Dellaportas P., Stephens D. A., 1995, *Biometrics*, 51, 1085
 Dermer C. D., 2004, *ApJ*, 614, 284
 Fan Y.-Z., Wei D.-M., Zhang F.-W., Zhang B.-B., 2012, *ApJL*, 755, L6
 Gelman A., 2006, *Bayesian analysis*, 1, 515
 Ghirlanda G., Nava L., Ghisellini G., 2010, *A&A*, 511, 43
 Giannios D., 2006, *A&A*, 457, 763
 Golenetskii S. V., Mazets E. P., Aptekar R. L., Ilinskii V. N., 1983, *Nature*, 306, 451
 Greiner J., 2011, *GCN Circular*
 Guiriec S., et al., 2013, *ApJ*, 770, 32
 Guiriec S., et al., 2015, *ApJ*
 Hunter J. D., 2007, *Computing In Science & Engineering*, 9, 90
 Iyyani S., Ryde F., Burgess J. M., Pe’er A., egué D. B., 2015, *arXiv.org*
 Kargatis V., 1994, *AAS*, 185, 1508
 Kelly B. C., 2007, *ApJ*, 665, 1489
 Kocevski D., 2012, *ApJ*, 747, 146
 López-Cámara D., Morsony B. J., Lazzati D., 2014, *MNRAS*, 442, 2202
 Lu R. J., Hou S. J., Liang E.-W., 2010, *ApJ*, 720, 1146
 Lundman C., Pe’er A., Ryde F., 2014, *MNRAS*, 440, 3292
 Mandel K. S., Narayan G., Kirshner R. P., 2011, *ApJ*, 731, 120
 March M. C., Trotta R., Berkes P., Starkman G. D., Vaudrevange P. M., 2011, *MNRAS*, 418, 2308
 Massaro F., Cutini S., Conciatore M. L., Tramacere A., 2007, *arXiv.org*, pp 84–87
 Pe’er A., Meszaros P., Rees M. J., 2005, *ApJ*, 635, 476
 Preece R., Burgess J. M., et al., 2014, *Science*, 343, 51
 Press W. H., 2007, *Numerical Recipes 3rd Edition. The Art of Scientific Computing*, Cambridge University Press
 Ryde F., Bjornsson C.-I., Kaneko Y., Meszaros P., Preece R., Battelino M., 2006, *ApJ*, 652, 1400
 Ryde F., et al., 2010, *ApJL*, 709, L172
 Sanders N. E., et al., 2015, *ApJ*, 799, 208
 Waskom M., et al., 2015, *seaborn: v0.6.0 (June 2015)*
 Yonetoku D., Murakami T., Nakamura T., 2004, *ApJ*
 Zhang B., Meszaros P., 2002, *ApJ*
 Zhang B.-B., Uhm Z. L., Connaughton V., Briggs M. S., Zhang B., 2015, *arXiv.org*, p. 5858
 Zhang Z. B., Chen D. Y., 2012, *ApJ*, 755, 55

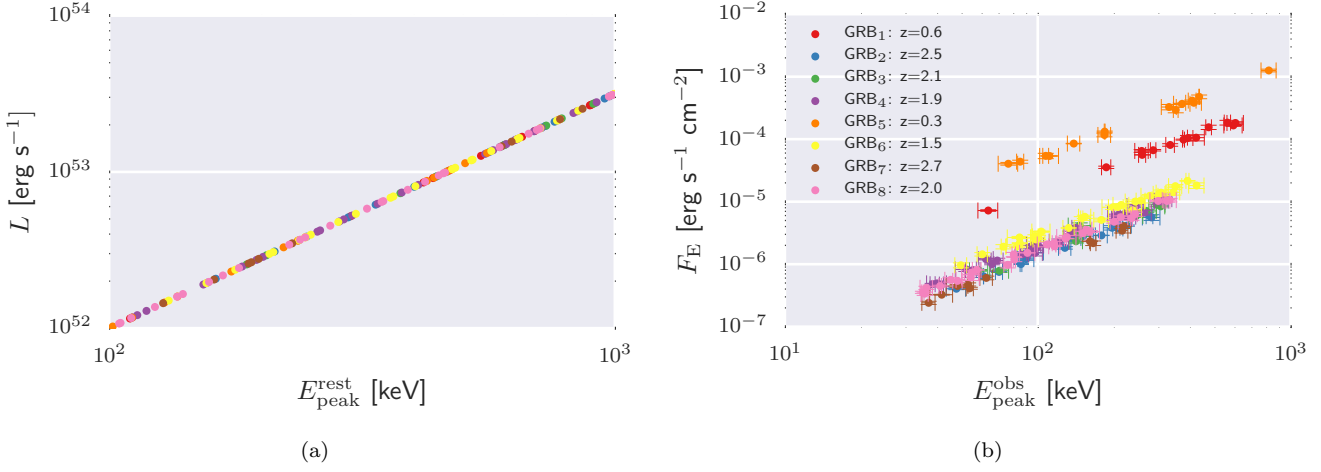


Figure 2. The simulated rest-frame (left) and observer-frame (right) data from *Mod A*

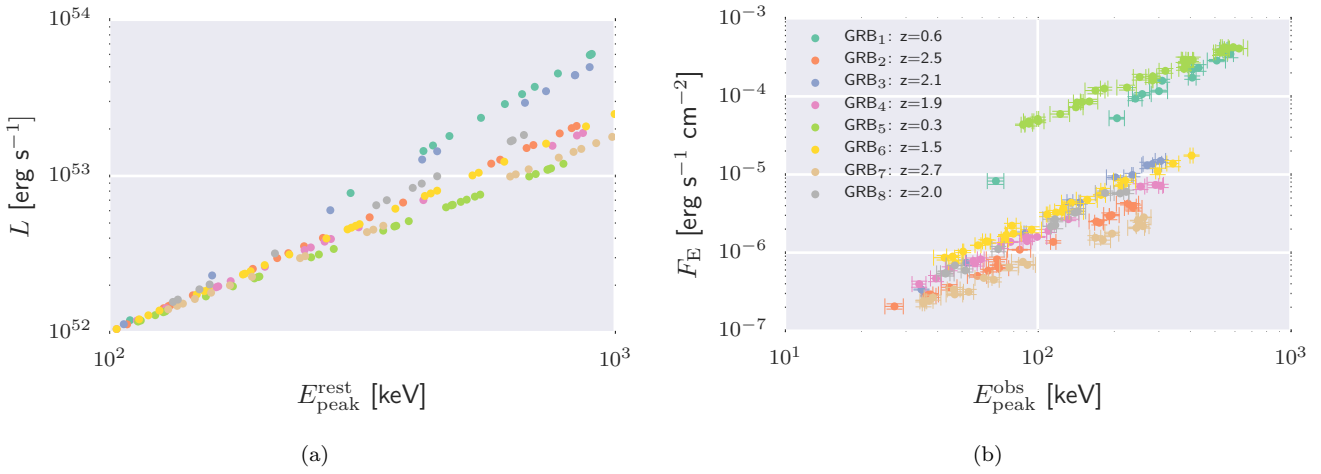


Figure 3. The simulated rest-frame (left) and observer-frame (right) data from *Mod B*

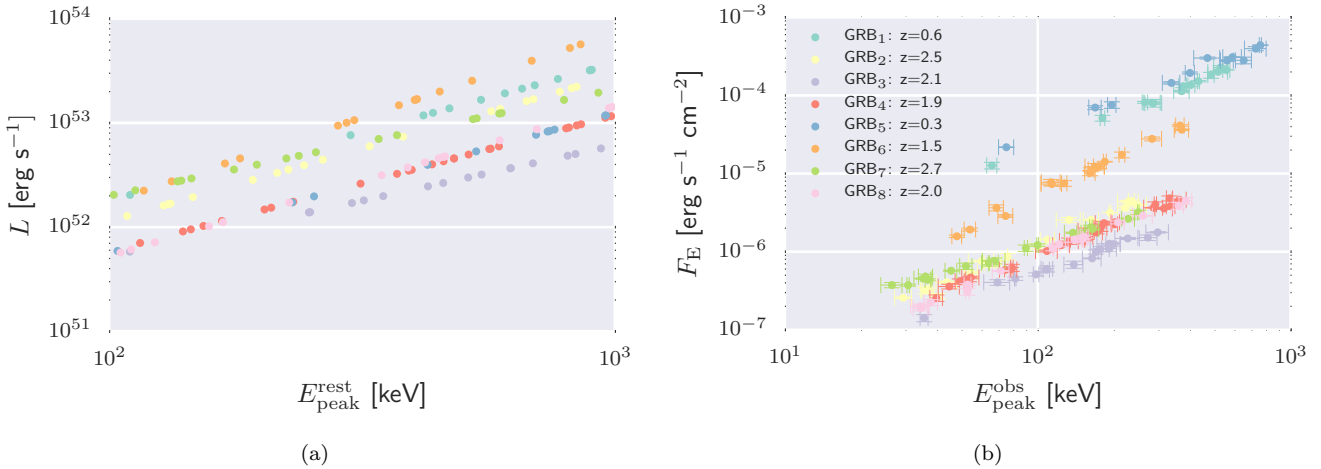


Figure 4. The simulated rest-frame (left) and observer-frame (right) data from *Mod C*

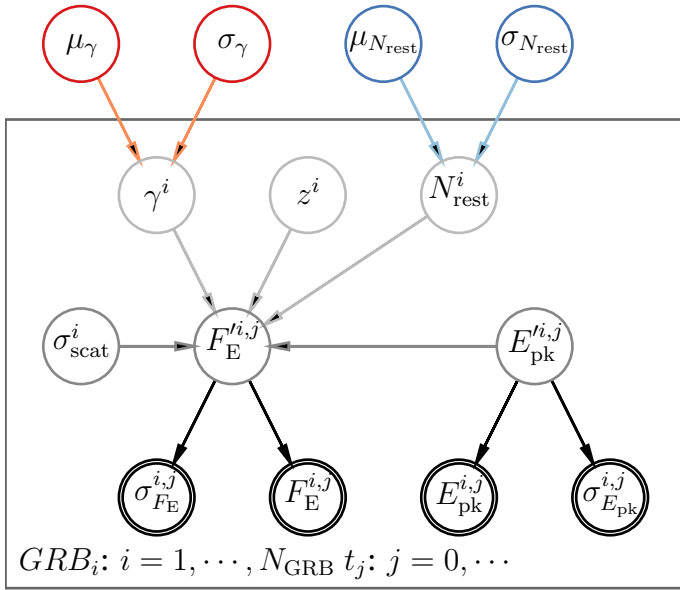


Figure 1. Graphical representation of the Bayesian hierarchical models. For visual simplicity, logarithmic quantities in the linear Equation 5 are represented as $Q = \log(Q)$ as well as with their associated priors. Here, i runs over the number of GRBs (N_{GRB}) in the data set and j is the time-evolution iterator. *Mod A* is the full model while *Mod B* and *Mod C* are represented by disregarding the *red* and then the *blue* hyper-priors respectively.

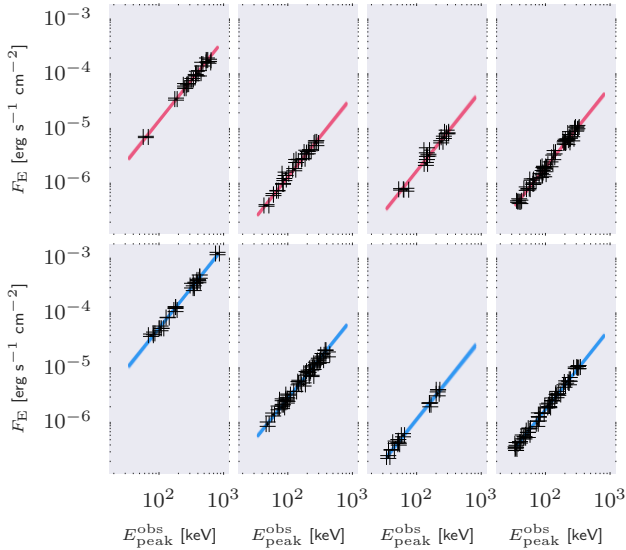


Figure 5. The reconstructed observer-frame GCs from simulations of *Mod A* assuming four redshifts are known. The *red* lines map out the posterior of known redshift GRBs while *blue* maps out the posterior of unknown redshift GRBs. The plots correspond to GRB₁ - GRB₈ from top-left to bottom right respectively.

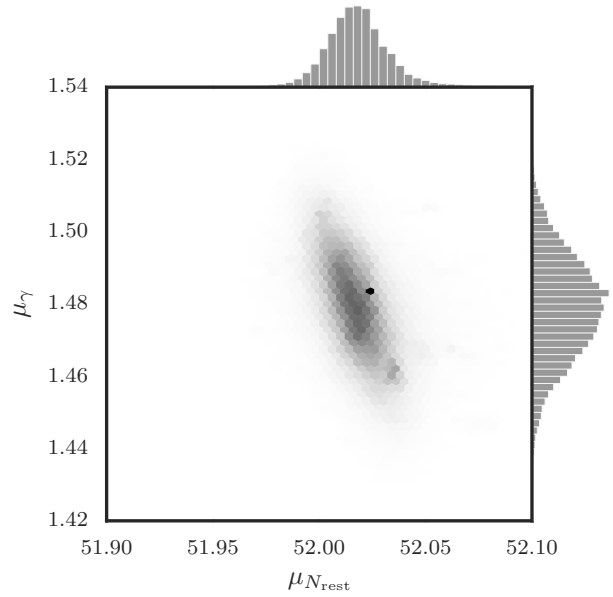


Figure 6. The distributions of hyper-parameters for N_{rest}^i and γ^i for simulations of *Mod A*.

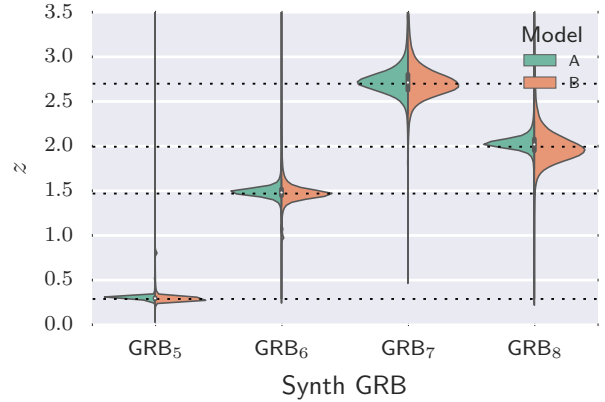


Figure 7. Comparing the redshift estimations of *Mod A* and *Mod B*. In general, *Mod A* has tighter constraints on redshift estimation. The dashed lines indicate the simulated values.

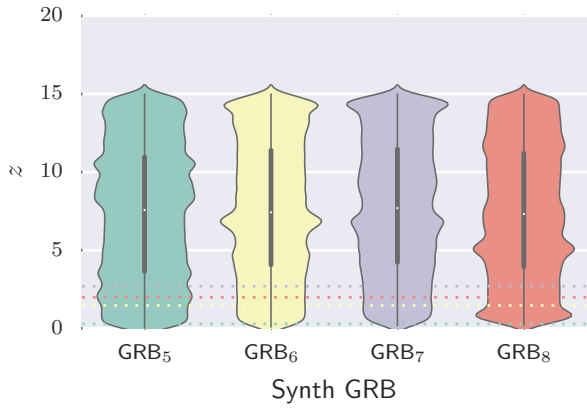
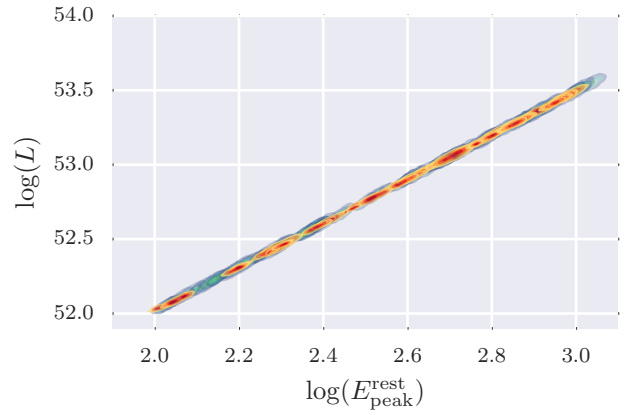
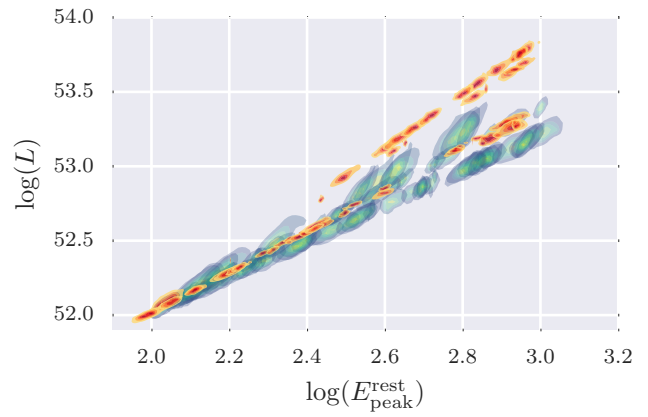


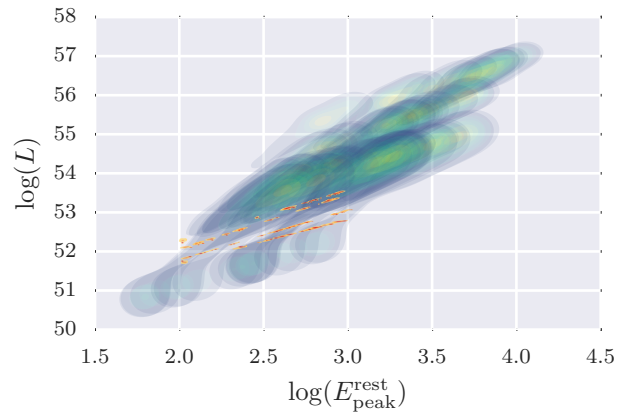
Figure 8. The estimated distributions of unknown redshifts for simulations of *Mod C*. The dashed lines indicate the simulated values.



(a)



(b)



(c)

Figure 9. The reconstructed rest-frame Golenetskii correlations from data simulated and fit with (from top to bottom) *Mod A*, *Mod B*, and *Mod C*. The fits reconstruct the simulated relations (Figures 2 - 4) for both GRBs with known (*yellow-red*) and unknown (*blue-green*) redshift excellently with the exception of *Mod C* which cannot determine the relation for GRBs without known redshift.

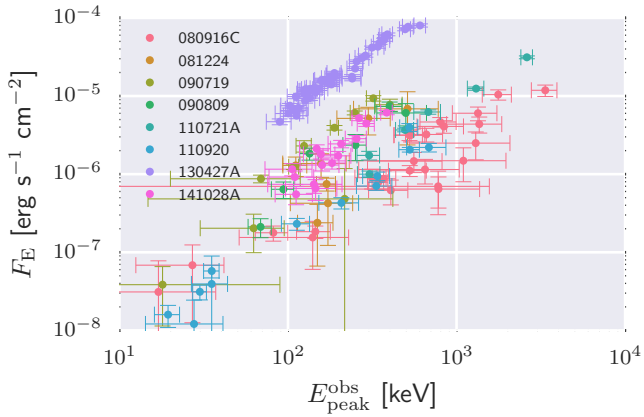


Figure 10. The observer-frame GCs for real GRBs in our sample.

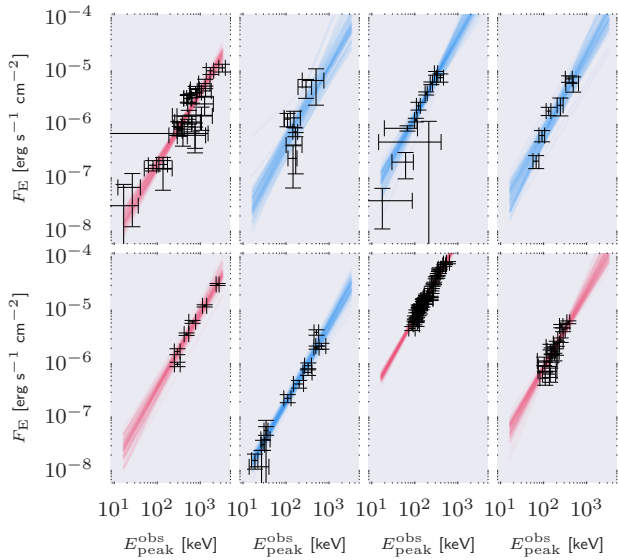


Figure 11. The reconstructed observer-frame GCs for real data fit with *Mod A*. The *red* lines map out the posterior of known redshift GRBs while *blue* maps out the posterior of unknown redshift GRBs. The plots from top-left to bottom right display GRBs 080916C, 081224A, 090719A, 090809A, 110721A, 110920A, 130427A, and 141028A respectively.

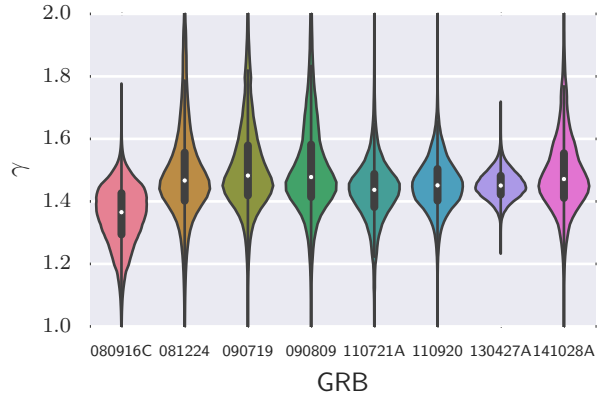


Figure 12. The estimated distributions of γ^i for real data fit with *Mod A*.

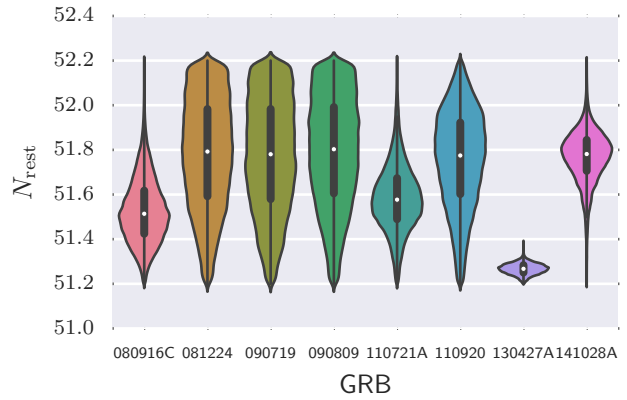


Figure 13. The estimated distributions of N_{rest}^i for real data fit with *Mod A*.

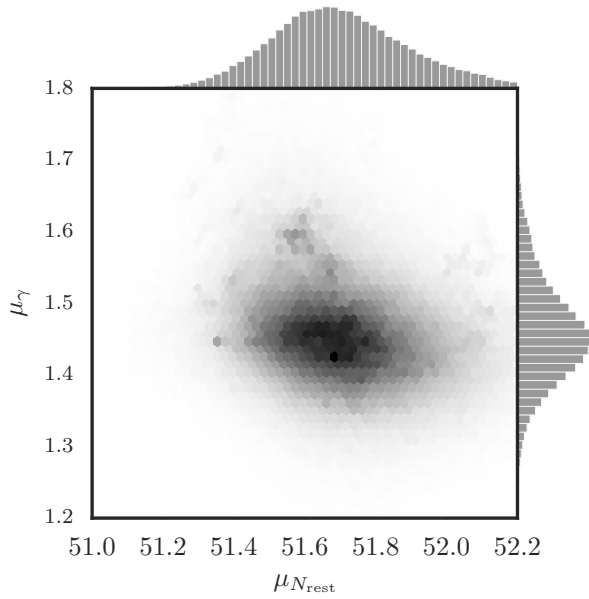


Figure 14. The distributions of hyper-parameters for N_{rest}^i and γ^i for real data fit with *Mod A*.

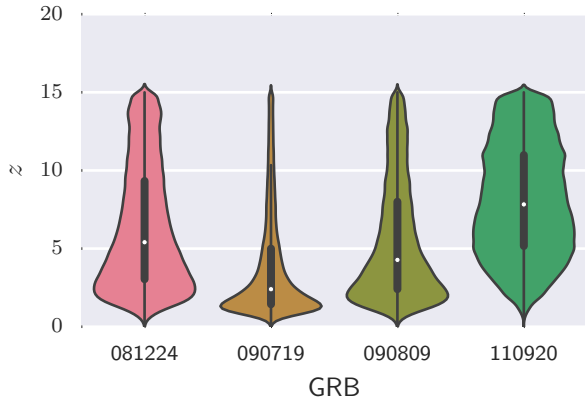


Figure 15. The estimated distributions of unknown redshifts for real data fit with *Mod A*

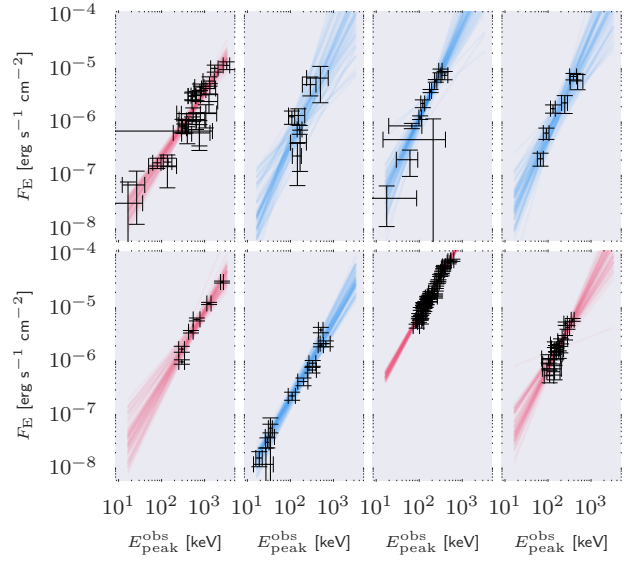


Figure 16. Same as Figure 11 but for *Mod B*.

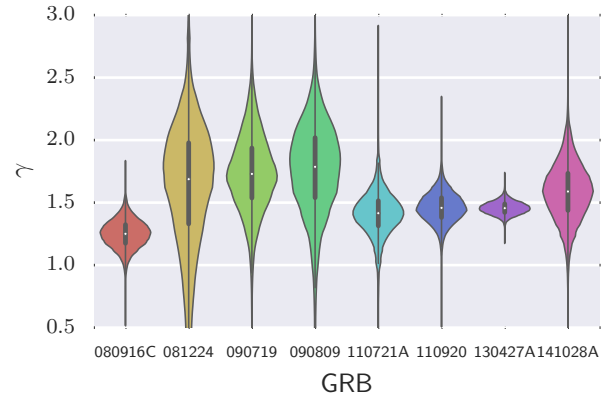


Figure 17. Same as Figure 12 but for *Mod B*.

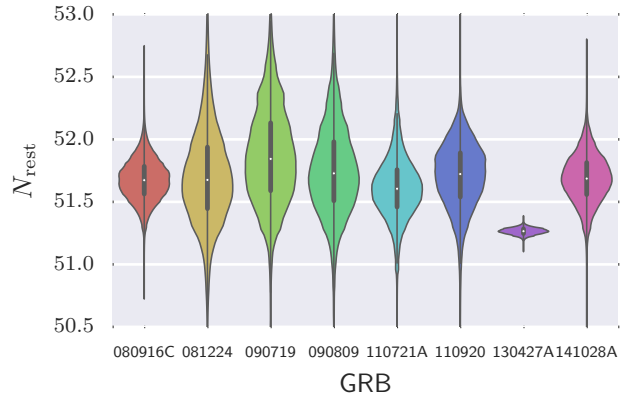


Figure 18. Same as Figure 13 but for *Mod B*.

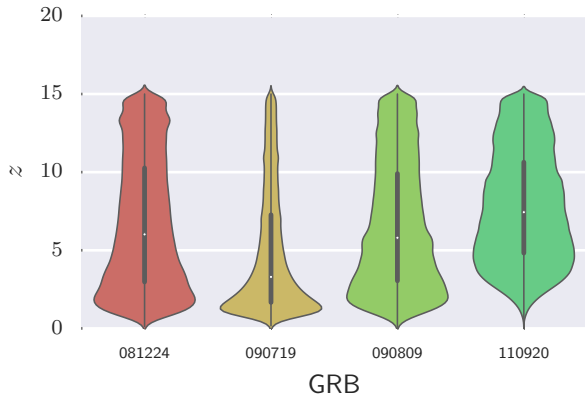


Figure 19. Same as Figure 15 but for *Mod B*.

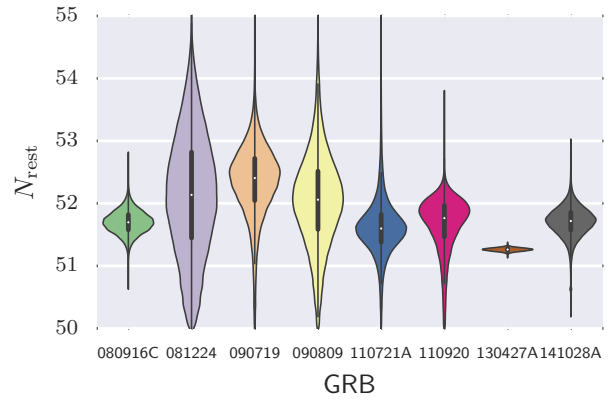


Figure 22. Same as Figure 13 but for *Mod C*.

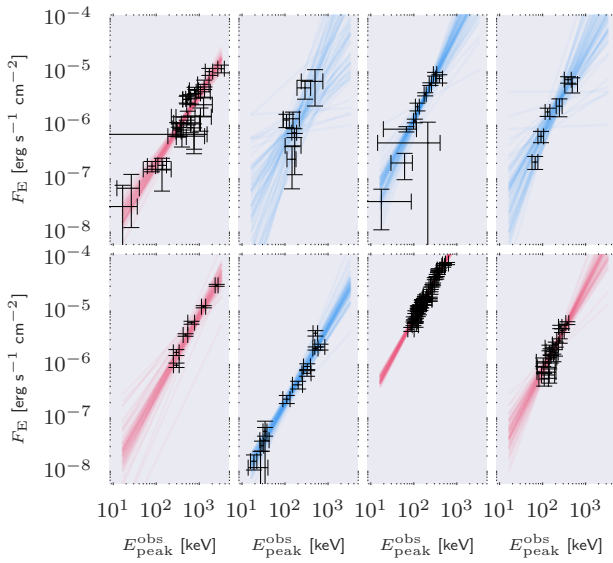


Figure 20. Same as Figure 11 but for *Mod C*.

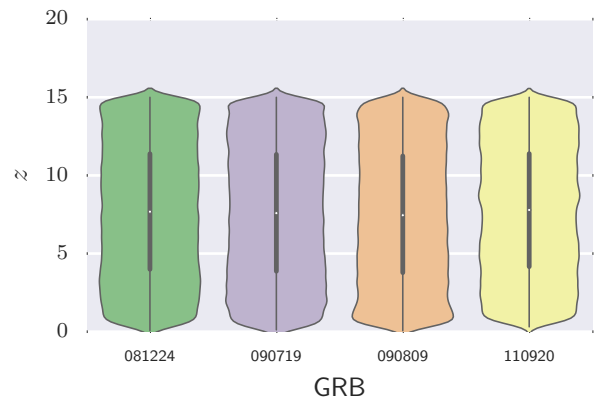


Figure 23. Same as Figure 15 but for *Mod C*.

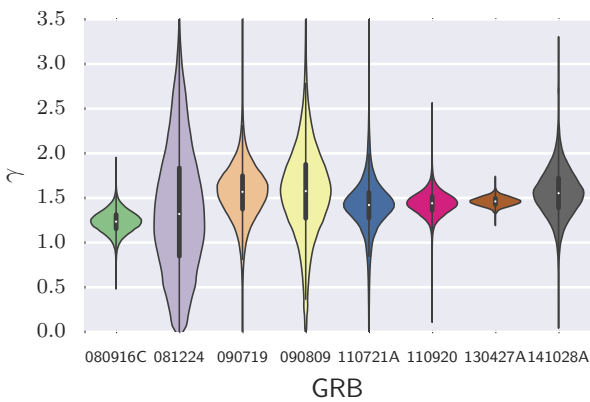


Figure 21. Same as Figure 12 but for *Mod C*.

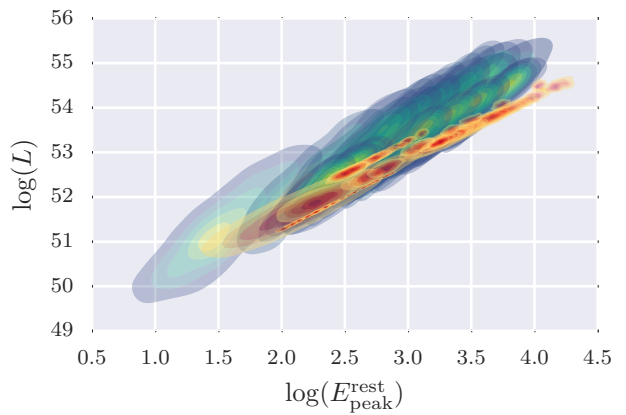
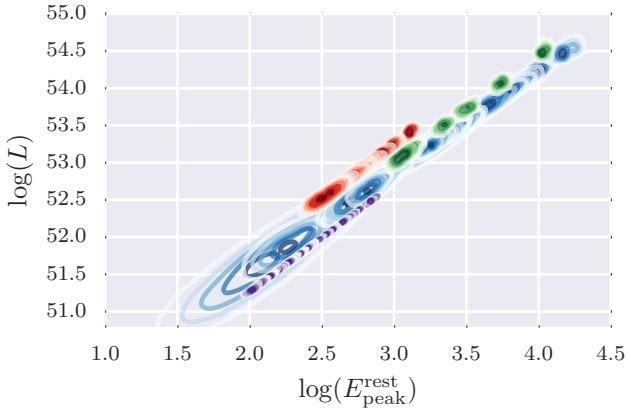
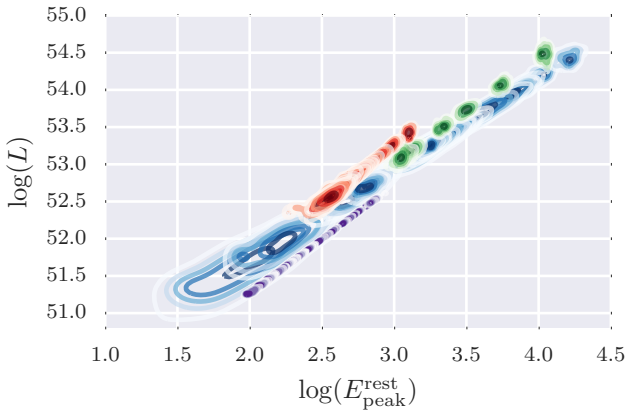


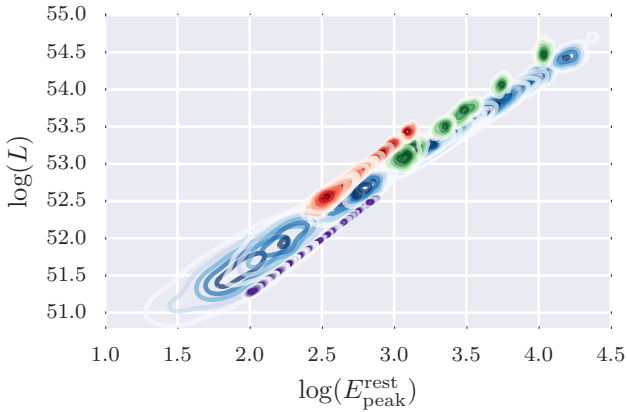
Figure 24. The rest-frame GC for real GRBs fit with *Mod A* demonstrating the difference in constraints for GRBs with known redshift (yellow-red) and without known redshift (blue-green).



(a)



(b)



(c)

Figure 25. From top to bottom, the predicted rest-frame Golenetskii correlations for GRBs with known redshift from *Mod A-Mod C* respectively. GRBs 080916C (blue), 110721A (red), 130427A (purple), and 141028A (purple) are displayed. Take note of the differences in amplitude of the GCs even though all are fit with different models.

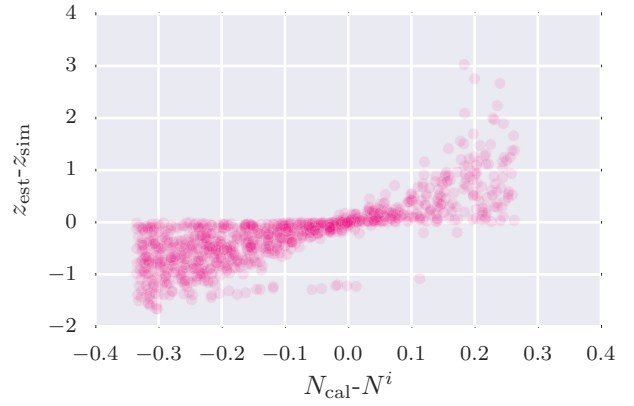


Figure 26. The distribution of miscalculated redshifts as a function of the distance of the simulated N_{rest} from N_{cal} for fits performed with FITEXY showing a clear relation of underestimated redshift when the true N_{rest} is greater than N_{cal} as is observed in the real data.

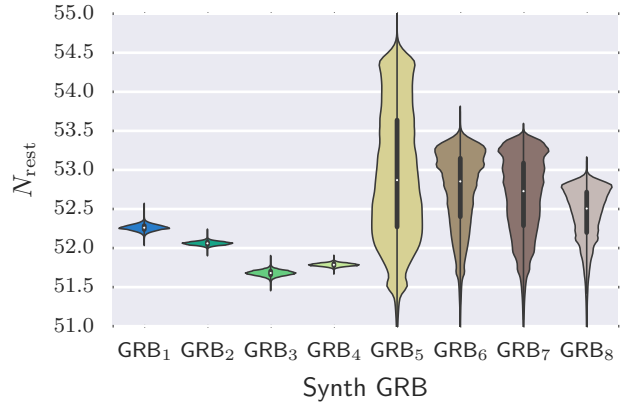


Figure 27. The N_{rest}^i for GCs simulated from *Mod C* but fit with *Mod A*. GRBs with unknown redshift have unconstrained N_{rest} similar to what is observed in real data.

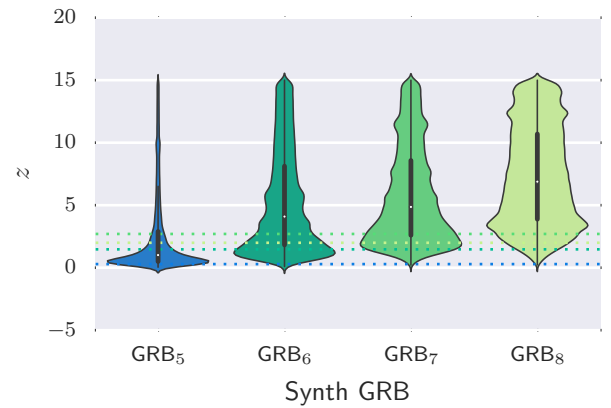


Figure 28. The predicted z^i for GCs simulated from *Mod C* but fit with *Mod A*. GRBs with unknown redshift have unconstrained z similar to what is observed in real data (compare to Figure 15).

Table 1. Fit Results of *Mod A* on Simulations

Synth. GRB	z	$\langle z_{\text{est}} \rangle$	z_{est} 95% HDI	N_{rest}	$\langle N_{\text{rest,est}} \rangle$	$N_{\text{rest,est}}$ 95% HDI	γ	$\langle \gamma_{\text{est}} \rangle$	γ_{est} 95% HDI
GRB ₀	0.60	52.00	52.02	51.99 - 52.05	1.50	1.48	1.44 - 1.52
GRB ₁	2.48	52.00	52.02	51.99 - 52.04	1.50	1.48	1.45 - 1.52
GRB ₂	2.06	52.00	52.02	51.98 - 52.05	1.50	1.48	1.44 - 1.52
GRB ₃	1.85	52.00	52.01	51.99 - 52.04	1.50	1.48	1.44 - 1.51
GRB ₄	0.29	0.32	0.26 - 0.34	52.00	52.04	51.91 - 52.12	1.50	1.48	1.44 - 1.52
GRB ₅	1.47	1.57	1.27 - 1.75	52.00	52.03	51.92 - 52.14	1.50	1.47	1.43 - 1.51
GRB ₆	2.70	2.86	2.27 - 3.46	52.00	52.03	51.94 - 52.16	1.50	1.48	1.44 - 1.52
GRB ₇	1.99	2.13	1.74 - 2.43	52.00	52.03	51.91 - 52.12	1.50	1.49	1.46 - 1.52

Table 2. Fit Results from FITEXY on Simulated Data from *Mod A*

Synth. GRB	z	z_{est}	γ	γ_{est}
GRB ₀	0.60	0.57 ± 0.04	1.46 ± 0.05	1.50
GRB ₁	2.48	2.45 ± 0.14	1.49 ± 0.03	1.50
GRB ₂	2.06	2.11 ± 0.23	1.51 ± 0.06	1.50
GRB ₃	1.85	1.85 ± 0.06	1.48 ± 0.02	1.50
GRB ₄	0.29	0.29 ± 0.01	1.47 ± 0.03	1.50
GRB ₅	1.47	1.45 ± 0.05	1.48 ± 0.02	1.50
GRB ₆	2.70	2.70 ± 0.15	1.50 ± 0.03	1.50
GRB ₇	1.99	2.02 ± 0.06	1.51 ± 0.02	1.50

Table 3. Fit Results of *Mod B* on Simulations

Synth. GRB	z	$\langle z_{\text{est}} \rangle$	z_{est} 95% HDI	N_{rest}	$\langle N_{\text{rest,est}} \rangle$	$N_{\text{rest,est}}$ 95% HDI	γ	$\langle \gamma_{\text{est}} \rangle$	γ_{est} 95% HDI
GRB ₀	0.60	52.00	52.02	51.95 - 52.11	1.87	1.83	1.71 - 1.93
GRB ₁	2.48	52.00	52.01	51.98 - 52.05	1.43	1.40	1.34 - 1.46
GRB ₂	2.06	52.00	52.01	51.97 - 52.06	1.79	1.75	1.68 - 1.83
GRB ₃	1.85	52.00	52.02	51.98 - 52.05	1.36	1.34	1.27 - 1.41
GRB ₄	0.29	0.35	0.19 - 0.55	52.00	52.08	51.76 - 52.65	1.20	1.20	1.16 - 1.25
GRB ₅	1.47	1.69	0.96 - 2.35	52.00	52.05	51.71 - 52.34	1.40	1.37	1.33 - 1.42
GRB ₆	2.70	3.05	2.22 - 5.99	52.00	52.06	51.92 - 52.55	1.26	1.20	1.13 - 1.26
GRB ₇	1.99	2.32	1.56 - 4.64	52.00	52.06	51.89 - 52.50	1.54	1.52	1.39 - 1.64

Table 4. Fit Results from FITEXY on Simulated Data from *Mod B*

Synth. GRB	z	z_{est}	N	γ	γ_{est}
GRB ₀	0.60	0.54 ± 0.05	52.00	1.87	1.87 ± 0.06
GRB ₁	2.48	2.16 ± 0.11	52.00	1.43	1.41 ± 0.03
GRB ₂	2.06	1.81 ± 0.06	52.00	1.79	1.77 ± 0.02
GRB ₃	1.85	1.62 ± 0.07	52.00	1.36	1.34 ± 0.03
GRB ₄	0.29	0.26 ± 0.01	52.00	1.20	1.21 ± 0.02
GRB ₅	1.47	1.29 ± 0.03	52.00	1.40	1.38 ± 0.01
GRB ₆	2.70	2.37 ± 0.06	52.00	1.26	1.24 ± 0.02
GRB ₇	1.99	1.73 ± 0.11	52.00	1.54	1.52 ± 0.04

Table 5. Fit Results of *Mod C* on Simulations

Synth. GRB	z	$\langle z_{\text{est}} \rangle$	z_{est} 95% HDI	N_{rest}	$\langle N_{\text{rest,est}} \rangle$	$N_{\text{rest,est}}$ 95% HDI	γ	$\langle \gamma_{\text{est}} \rangle$	γ_{est} 95% HDI
GRB ₀	0.60	52.26	52.26	52.18 - 52.34	1.32	1.32	1.22 - 1.42
GRB ₁	2.48	52.06	52.06	52.00 - 52.10	1.40	1.40	1.33 - 1.49
GRB ₂	2.06	51.72	51.69	51.61 - 51.76	1.06	1.14	1.03 - 1.26
GRB ₃	1.85	51.77	51.79	51.74 - 51.83	1.31	1.27	1.21 - 1.33
GRB ₄	0.29	7.43	0.04 - 14.18	51.75	53.96	52.56 - 54.71	1.35	1.27	1.16 - 1.38
GRB ₅	1.47	7.66	0.52 - 14.61	52.24	52.95	51.87 - 53.48	1.63	1.57	1.48 - 1.66
GRB ₆	2.70	7.79	1.04 - 15.00	52.30	52.84	51.54 - 53.47	1.02	0.99	0.94 - 1.04
GRB ₇	1.99	7.48	0.65 - 14.62	51.72	52.37	51.08 - 52.92	1.44	1.32	1.24 - 1.40

 Table 6. Fit Results from *FITEXY* on Simulated Data from *Mod C*

Synth. GRB	z	z_{est}	N	γ	γ_{est}
GRB ₀	0.60	0.26 ± 0.02	52.26	1.32	1.32 ± 0.04
GRB ₁	2.48	1.14 ± 0.04	52.06	1.40	1.40 ± 0.02
GRB ₂	2.06	1.65 ± 0.11	51.72	1.06	1.15 ± 0.05
GRB ₃	1.85	1.29 ± 0.05	51.77	1.31	1.28 ± 0.03
GRB ₄	0.29	0.21 ± 0.01	51.75	1.35	1.29 ± 0.03
GRB ₅	1.47	0.55 ± 0.03	52.24	1.63	1.59 ± 0.04
GRB ₆	2.70	0.99 ± 0.02	52.30	1.02	1.00 ± 0.02
GRB ₇	1.99	1.38 ± 0.06	51.72	1.44	1.33 ± 0.03

 Table 7. Fit results from *Mod A* on Real Data

GRB	z	$\langle z_{\text{est}} \rangle$	z_{est} 95% HDI	$\langle N_{\text{rest,est}} \rangle$	$N_{\text{rest,est}}$ 95% HDI	$\langle \gamma_{\text{est}} \rangle$	γ_{est} 95% HDI
080916C	4.24	51.53	51.26 - 51.82	1.36	1.16 - 1.53
081224	...	6.37	0.98 - 14.02	51.88	51.19 - 52.59	1.49	1.20 - 1.90
090719	...	3.80	0.35 - 11.66	52.00	51.23 - 52.89	1.51	1.25 - 1.85
090809	...	5.50	0.66 - 13.28	51.93	51.21 - 52.68	1.51	1.22 - 1.87
110721A	3.20	51.58	51.25 - 51.91	1.43	1.22 - 1.63
110920	...	8.08	2.61 - 14.95	51.73	51.19 - 52.19	1.45	1.29 - 1.63
130427A	0.34	51.27	51.22 - 51.31	1.45	1.37 - 1.54
141028A	2.33	51.77	51.53 - 51.98	1.49	1.26 - 1.77

 Table 8. Fit results from *Mod B* on Real Data

GRB	z	$\langle z_{\text{est}} \rangle$	z_{est} 95% HDI	$\langle N_{\text{rest,est}} \rangle$	$N_{\text{rest,est}}$ 95% HDI	$\langle \gamma_{\text{est}} \rangle$	γ_{est} 95% HDI
080916C	4.24	51.67	51.35 - 52.00	1.25	1.03 - 1.47
081224A	...	6.73	0.73 - 14.22	51.71	50.91 - 52.58	1.64	0.43 - 2.50
090719A	...	4.84	0.46 - 13.21	51.87	51.16 - 52.67	1.73	1.14 - 2.39
090809A	...	6.61	0.82 - 14.17	51.75	51.06 - 52.52	1.76	1.00 - 2.48
110721A	3.20	51.61	51.09 - 52.17	1.41	1.01 - 1.75
110920A	...	7.80	2.33 - 14.60	51.71	51.19 - 52.20	1.46	1.22 - 1.70
130427A	0.34	51.26	51.21 - 51.31	1.46	1.36 - 1.55
141028A	2.33	51.68	51.28 - 52.06	1.59	1.12 - 2.04

Table 9. Fit results from *Mod C* on Real Data

GRB	z	$\langle z_{\text{est}} \rangle$	z_{est} 95% HDI	$\langle N_{\text{rest,est}} \rangle$	$N_{\text{rest,est}}$ 95% HDI	$\langle \gamma_{\text{est}} \rangle$	γ_{est} 95% HDI
080916C	4.24	51.70	51.33 - 52.06	1.23	0.99 - 1.48
081224A	...	7.70	1.08 - 14.99	52.14	50.24 - 53.92	1.37	0.02 - 2.66
090719A	...	7.61	0.95 - 14.96	52.35	51.09 - 53.47	1.56	0.90 - 2.17
090809A	...	7.51	0.41 - 14.36	52.05	50.39 - 53.49	1.57	0.47 - 2.61
110721A	3.20	51.62	50.65 - 52.61	1.41	0.74 - 2.03
110920A	...	7.76	1.03 - 14.77	51.66	50.66 - 52.36	1.44	1.19 - 1.69
130427A	0.34	51.26	51.21 - 51.31	1.46	1.37 - 1.56
141028A	2.33	51.71	51.24 - 52.16	1.56	1.02 - 2.11

Table 10. FITEXY Results using all known redshift GRBs as Calibration Sources

GRB	z	z_{est}	γ_{est}
080916C	4.24	2.51 ± 0.50	1.39 ± 0.09
081224A	...	3.64 ± 583.90	3.05 ± 1.38
090719A	...	0.88 ± 0.22	1.80 ± 0.17
090809A	...	1.29 ± 0.53	1.80 ± 0.25
110721A	3.20	1.70 ± 0.33	1.44 ± 0.09
110920A	...	2.40 ± 0.34	1.50 ± 0.07
130427A	0.34	0.31 ± 0.02	1.52 ± 0.05
141028A	2.33	1.49 ± 0.68	1.91 ± 0.24

Table 11. Predicted Redshifts via FITEXY using individual GRBs as Calibration Sources

Calib. GRB	080916C ($z = 4.24$)	110721A ($z = 3.2$)	130427A ($z = 0.34$)	141028A ($z = 2.332$)
080916C	4.24 ± 1.27	2.75 ± 0.72	0.45 ± 0.03	2.71 ± 1.67
110721A	5.01 ± 1.66	3.20 ± 0.91	0.50 ± 0.04	3.33 ± 2.31
130427A	2.79 ± 0.58	1.88 ± 0.37	0.34 ± 0.02	1.68 ± 0.80
141028A	3.74 ± 1.32	2.45 ± 0.72	0.42 ± 0.03	2.33 ± 1.41

APPENDIX A: MARGINAL POSTERIOR DISTRIBUTIONS FROM SIMULATIONS

For completeness, I display the marginal posterior distributions of the simulations. Figures C1-C3 display the distributions from simulations of *Mod A*. Figures C4-C6 display the distributions of simulations from *Mod B*. Finally, Figures C7-C8 display the distributions of simulations from *Mod C*.

APPENDIX B: F_E ERROR PROPAGATION

In order to calculate the errors on F_E for a single component from a multi-component fit, one must recognize that in **RMFIT**, it is the total model that is fitted and therefore care must be taken to compute the individual component errors. Suppose we have a multi-component photon model fitted to data:

$$\mathcal{M}_T(\varepsilon; \vec{\theta}_T) = \mathcal{M}_A(\varepsilon; \vec{\theta}_A) + \mathcal{M}_B(\varepsilon; \vec{\theta}_B) \text{ ph}t \text{ s}^{-1} \text{ cm}^{-2} \text{ keV}^{-1} \quad (\text{B1})$$

where \mathcal{M}_T , \mathcal{M}_A , and \mathcal{M}_B are the total photon model, and photon models A and B respectively with parameter vectors $\vec{\theta}_i$. Since we measure \mathcal{M}_T , then computing $F_{E,A}$ is equivalent to

$$F_{E,A} = \int d\varepsilon \left[\varepsilon \mathcal{M}_T(\varepsilon; \vec{\theta}_T) - \mathcal{M}_B(\varepsilon; \vec{\theta}_B) \right] \text{ keV s}^{-1}. \quad (\text{B2})$$

Hence, the errors on the single A component are correlated to the total model and second B component. Let $\sigma_{T,ij}^2$ be the covariance matrix from the spectral fit, $A_i = \frac{\partial F_{E,A}}{\partial \theta_i} |_{\langle \theta_i \rangle}$. Proceeding with the typical Taylor expansion error propagation scheme, the variance of $F_{E,A}$ is

$$\sigma_{F_{E,A}}^2 = \sum_i \sum_j A_i \sigma_{T,ij}^2 A_j. \quad (\text{B3})$$

If one calculates the error on a component's F_E by considering only the errors on its parameters, then the errors F_E become much larger than the method demonstrated here which can lead to unrealistic flexibility when fitting GCs by either the Bayesian model or **FITEXY**. To demonstrate the difference in the techniques we compare the error of the non-thermal component F_E for the fourth time interval of GRB080916C from both methods. The $F_E = 3.14 \cdot 10^{-6}$ erg s⁻¹ and $\sigma_{F_E} = 4.53 \cdot 10^{-7}$ erg s⁻¹ from the method demonstrated here and $\sigma_{F_E} = 1.18 \cdot 10^{-6}$ erg s⁻¹ from the method that does not take into account the full parameter correlations. The order of magnitude difference may explain the differences between Figure 10 herein and Figure 15 of Guiriec et al. (2015).

APPENDIX C: STAN MODEL CODE

The following code demonstrates the Stan implementation of *Mod A*. The code takes the known $E_{\text{peak}}^{\text{obs}}$ and F_E with their associated errors (**Ep_obs**, **FE_obs**, **Ep_sig**, **FE_sig**) as well as the pre-calculated rest-frame quantities (**Nz**) and known redshifts (**z_known**). A warmup/sample split of 1/2 is taken with 30K iterations which insured convergence.

```

data{
  int<lower=0> N;
  int<lower=0> Nunknown;
  int<lower=0> Ngroups;
  vector[N] z_known;
  vector[N] Nz;
  int group[N];
  int unknown_group[N];
  int known[N];
  real maxSlope;
  vector[N] FE_obs;
  vector[N] Ep_obs;
  vector[N] Ep_sig;
  vector[N] FE_sig;
}

parameters {
  vector<lower=-2,upper=5>[N] Ep_true;
  vector[N] FE_true;
  vector<lower=50>[Ngroups] Nrest;
  vector<lower=0>[Ngroups] gamma;
  vector<lower=0.0,upper=15>[Nunknown] z;
  vector<lower=0>[Ngroups] int_scatter_sq;
  real<lower=0> gamma_mu_meta;
  real Nrest_mu_meta;
  real<lower=0> gamma_sig_meta;
  real<lower=0> Nrest_sig_meta;
}

transformed parameters {
  vector<lower=0>[Ngroups] int_scatter;

  for(i in 1:Ngroups){
    int_scatter[i] <- sqrt(int_scatter_sq[i]);
  }
}

model {
  gamma_sig_meta ~ cauchy(0., 2.5);
  Nrest_sig_meta ~ cauchy(0., 2.5);
  gamma_mu_meta
  ~ normal(0, maxSlope);
  Nrest_mu_meta ~ normal(52, 5);
  gamma ~ normal(gamma_mu_meta, gamma_sig_meta);
  Nrest ~ normal(Nrest_mu_meta, Nrest_sig_meta);
  int_scatter_sq ~ cauchy(0, 2.5)
  z ~ uniform(0, 15);
  Ep_true ~ uniform(-2, 5);
  Ep_obs ~ normal(Ep_true, Ep_sig);

  for(i in 1:N){

```

```

if (known[i] == 0){
  FE_true[i] ~ normal( Nrest[group[i]] -
    ( 1.099 +
    2*log10( DL( z[unknown_group[i]]))) +
    gamma[group[i]]*
    (log10(1+z[unknown_group[i]])) +
    Ep_true[i]-2), int_scatter[group[i]]);
}

else{
  FE_true[i] ~ normal(Nrest[group[i]] -
    Nz[i] + gamma[group[i]] *
    (log10(1+z_known[i])) +
    Ep_true[i]-2), int_scatter[group[i]]);
}
}
FE_obs ~ normal(FE_true, FE_sig);
}

```

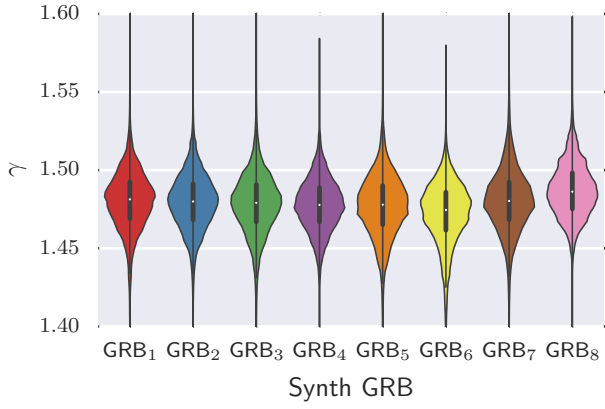


Figure C1. The estimated distributions of γ^i for simulations of *Mod A*.

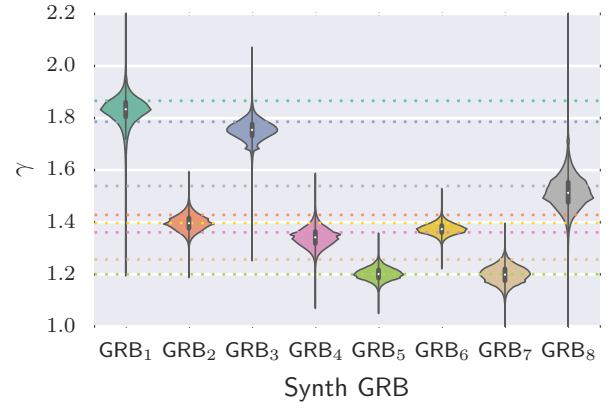


Figure C4. The estimated distributions of γ^i for simulations of *Mod B*.

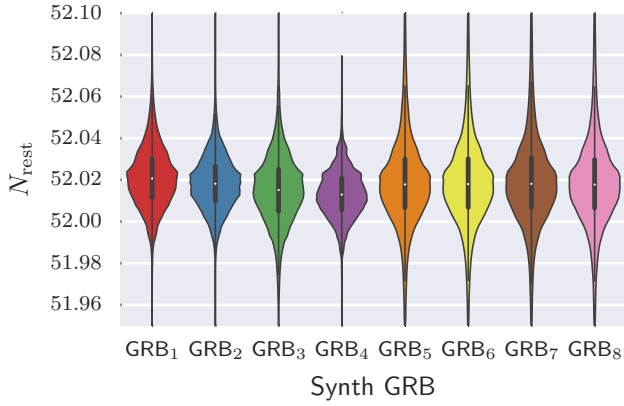


Figure C2. The estimated distributions of N_{rest}^i for simulations of *Mod A*.

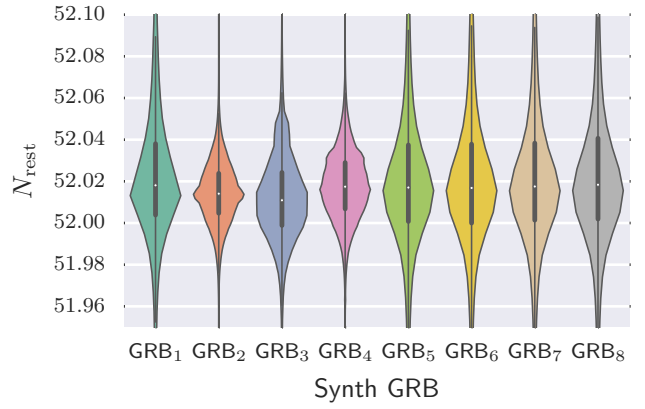


Figure C5. The estimated distributions of N_{rest}^i for simulations of *Mod B*.

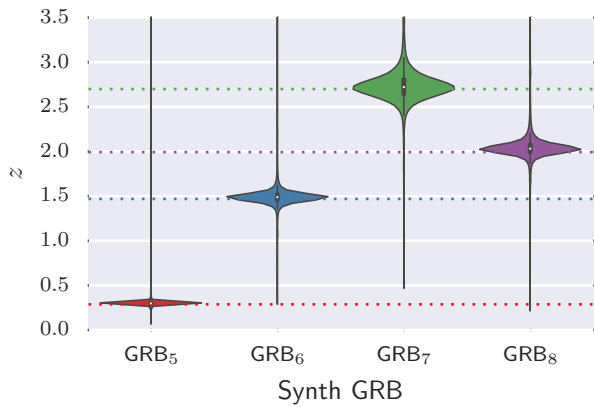


Figure C3. The estimated distributions of unknown redshifts for simulations of *Mod A*. The dashed lines indicate the simulated values.

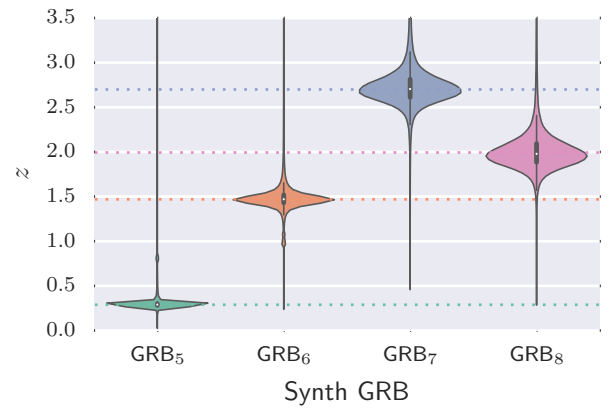


Figure C6. The estimated distributions of unknown redshifts for simulations of *Mod B*. The dashed lines indicate the simulated values.

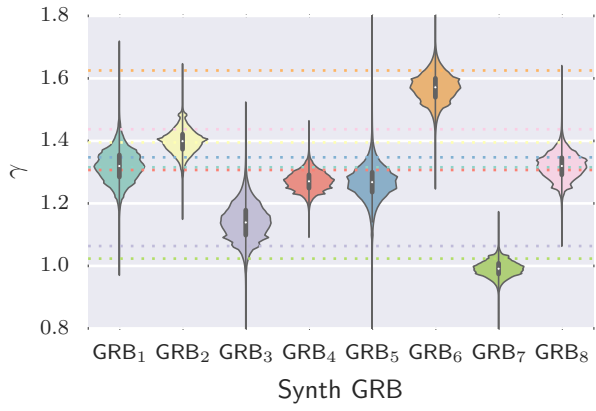


Figure C7. The estimated distributions of γ^i for simulations of *Mod C*.

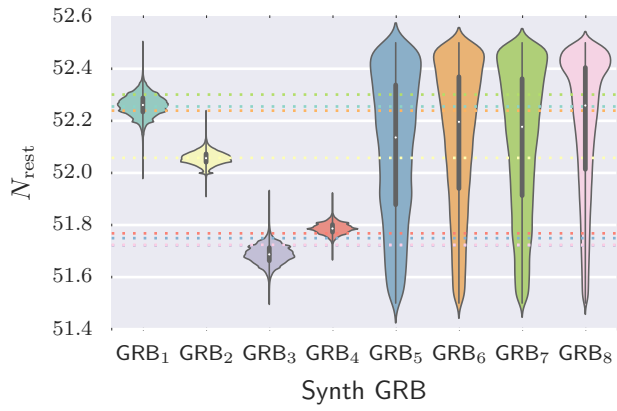


Figure C8. The estimated distributions of N_{rest}^i for simulations of *Mod C*.